Direct Observations of Particle Dynamics in Magnetized Collisionless Shock Precursors in Laser-Produced Plasmas

D. B. Schaeffer,[1,*] W. Fox,[1,2] R. K. Follett,[3] G. Fiksel,[4] C. K. Li,[5] J. Matteucci,[1] A. Bhattacharjee,[1,2] and K. Germaschewski[6]
[1]*Department of Astrophysical Sciences, Princeton University, Princeton, New Jersey 08540, USA*
[2]*Princeton Plasma Physics Laboratory, Princeton, New Jersey 08543, USA*
[3]*Laboratory for Laser Energetics, University of Rochester, Rochester, New York 14623, USA*
[4]*Center for Ultrafast Optical Science, University of Michigan, Ann Arbor, Michigan 48109, USA*
[5]*Plasma Science and Fusion Center, Massachusetts Institute of Technology, Cambridge, Massachusetts, USA*
[6]*Space Science Center, University of New Hampshire, Durham, New Hampshire 03824, USA*

(Received 16 November 2018; revised manuscript received 22 May 2019)

We present the first laboratory observations of time-resolved electron and ion velocity distributions in magnetized collisionless shock precursors. Thomson scattering of a probe laser beam was used to observe the interaction of a laser-driven, supersonic piston plasma expanding through an ambient plasma in an external magnetic field. From the Thomson-scattered spectra we measure time-resolved profiles of electron density, temperature, and ion flow speed, as well as spatially resolved magnetic fields from proton radiography. We observe direct evidence of the coupling between piston and ambient plasmas, including the acceleration of ambient ions driven by magnetic and pressure gradient electric fields, and deformation of the piston ion flow, key steps in the formation of magnetized collisionless shocks. Even before a shock has fully formed, we observe strong density compressions and electron heating associated with the pileup of piston ions. The results demonstrate that laboratory experiments can probe particle velocity distributions relevant to collisionless shocks, and can complement, and in some cases overcome, the limitations of similar measurements undertaken by spacecraft missions.

DOI:

Collisionless shocks are commonly found in systems in which strongly driven flows interact with preexisting magnetic fields, including planetary bow shocks in the heliosphere [1–3] and astrophysical shocks in supernova remnants [4–6]. In collisionless plasmas, these shocks form on spatial scales much smaller than the collisional mean free path due to dissipation mediated by electromagnetic fields. For most observed shocks, the fast inflow of particles can only be managed through the magnetic reflection of some particles back upstream, resulting in complex interactions between populations of inflowing, reflected, and shocked ions and electrons that are not fully understood. Consequently, fundamental questions, such as how energy is partitioned between electrons and ions across a collisionless shock [7–9], remain unanswered.

A key method for addressing these questions is the direct probing of particle velocity distributions, which has primarily been undertaken through *in situ* measurements by spacecraft. These missions have yielded a wealth of information on shock physics [10], and have recently begun to address the question of energy partitioning [11] as improved diagnostics have allowed high-resolution sampling of velocity distributions. Even so, spacecraft remain fundamentally limited, as they rely on the inherently noisy process of sampling shock crossings through multiple orbits and have difficulty gauging large-scale, 3D effects due to undersampling [12,13]. Laboratory experiments, with reproducible and controllable plasma conditions, can complement and overcome some of these limitations to help address fundamental questions [14], and have recently extended the regimes of magnetized shock formation to strongly driven laser plasmas [15,16]. Moreover, velocity distributions can be similarly probed in the laboratory by measuring the Thomson scattering of light off plasma waves [17,18]. Early experiments [19,20] pioneered the use of Thomson scattering to study magnetized shocks, but were limited to a sparse sampling of the electron velocity distribution. Recent experiments have used this diagnostic to study velocity distributions in collisional shocks [21,22] and in unmagnetized collisionless counterstreaming flows [23,24].

In this Letter, we present the first laboratory observations of temporally resolved electron and ion velocity distributions in magnetized collisionless shock precursors. The distributions were acquired through Thomson scattering of a probe laser that diagnosed the interaction of a laser-driven, supersonic piston plasma expanding through an ambient plasma in an external magnetic field. Spatially resolved 2D proton radiography images of the magnetic field were also acquired. We directly observe the coupling between the piston and ambient plasmas, including the acceleration of ambient ions by magnetic and pressure

gradient electric fields and the pileup of piston ions behind the resulting compressed magnetic field. These effects constitute a shock precursor [25], a key step in piston-driven shock formation, and are found to depend critically on the presence of the ambient plasma and background magnetic field. The results build on an experimental platform that has studied high-Mach-number magnetized collisionless shocks [16,26], laser-driven magnetic reconnection [27], and Weibel-mediated shocks [28].

Setup.—The experiments were carried out on the OMEGA laser facility [29] and are shown schematically in Fig. 1. The experiment utilizes two planar plastic (CH) targets and a set of copper coils to generate a magnetic field. The "piston" target is attached to the coils 3 mm from the target chamber center (TCC) and defines the experimental coordinate system, with $\hat{x}$ along the target normal, $\hat{y}$ parallel to the long edge, and $\hat{z}$ parallel to the short edge. A second "ambient" target is centered at TCC along $\hat{x}$ and offset 5 mm diagonally at a 45° angle. A background magnetic field is generated by the coils [30]. The initial field B_y has a peak strength of 10 T near the piston target and falls off like $1/x$ along $\hat{x}$, while it is nearly uniform across the target surface due to the elongated and stacked coil structure. A beam (351 nm, 100 J, 1 ns) incident on the ambient target creates an ambient plasma that expands through the background field. Twelve ns later, at time t_0, two drive beams (351 nm, 350 J, 2 ns) irradiate the piston target to generate a supersonic piston plasma, which expands through and sweeps up the ambient plasma and magnetic field. Note that while the ambient plasma also sweeps out magnetic flux, observations presented here and elsewhere [27] indicate that the ambient plasma is at least partially magnetized at time t_0. This implies anomalously fast magnetic diffusion, which is not unprecedented and has been experimentally observed in other laser plasma experiments [31,32] where the magnetic cavity collapses on timescales much faster than dictated by Spitzer or Bohm diffusion.

The primary diagnostic was temporally resolved Thomson scattering using a 2ω probe beam (527 nm, 30-50 J, 2 ns) [33]. Scattered light from the probe beam was collected from a localized volume ($50 \times 50 \times 70$ μm^3) such that the probed wave vector $\mathbf{k} = \mathbf{k_i} - \mathbf{k_s}$ was directed along the piston expansion direction (i.e., along $\hat{x}$), where $\mathbf{k_i}$ is the incident wave vector and $\mathbf{k_s}$ is the scattered wave vector [Fig. 1(b)]. The scattering angle was 63°, yielding a scattering parameter $\alpha = 1/k\lambda_{de} \approx 1.5$ for typical plasma parameters (i.e., the collective regime). The collected light was split along two beam paths. One path measured light scattered from electron plasma waves (EPW), which can provide information on the electron density and temperature. The other path measured light scattered from ion acoustic waves (IAW), which can also diagnose the electron temperature, as well as the ion temperature and flow speed. The EPW and IAW signals were passed through spectrometers with wavelength resolutions

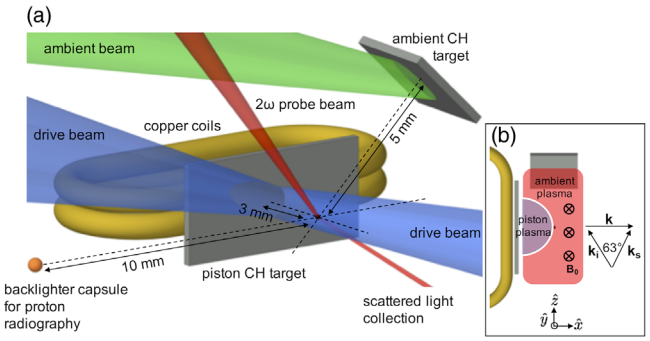

FIG. 1. (a) Experimental setup. A background magnetic field primarily directed along $\hat{y}$ is preimposed using current-carrying copper wires. A laser ablates a CH target to create an ambient plasma. Two drive beams then generate a CH piston plasma that expands through the ambient plasma to drive a shock. Temperature, density, and velocity are diagnosed in the $\hat{x}$ direction using Thomson scattering with a 2ω probe beam. Twenty beams (not shown) compress a DHe3 backlighter capsule to generate monoenergetic protons that probe the magnetic field structure in the x-y plane. (b) Top-down schematic view of the setup and Thomson scattering geometry.

of 0.5 and 0.05 nm, respectively, and imaged onto streak cameras with a temporal resolution of 50 ps. The location of the probed plasma ranged from 3 to 4 mm from the piston target along $\hat{x}$. The scattered signal was streaked for 2 ns starting 3 to 4.5 ns after t_0.

The magnetic field structure was measured using proton radiography [34]. A 420 μm diameter glass capsule filled with DHe3 was placed 10 mm from TCC along $\hat{z}$ and irradiated by 20 beams at $t_0 + 3$ ns. The resulting implosion produced 3 and 14.7 MeV protons as fusion byproducts, which passed through the plasma and were collected on CR-39 plates placed 154 mm from TCC (geometric magnification $M = 16.4$). The protons leave tracks in the CR-39 that correspond to a 2D map of proton deflections in the x-y plane, which can be converted to path-integrated magnetic field amplitudes.

Results.—Figure 2 shows streaked IAW spectra taken under three experimental configurations: (a) a magnetized piston-ambient interaction, (b) an unmagnetized piston-ambient interaction, and (c) a magnetized piston expansion. The EPW spectrum corresponding to Fig. 2(a) is shown in Fig. 3(a), and a proton radiograph taken under the same conditions is shown in Fig. 3(c). The ambient plasma was measured at TCC using Thomson scattering in the absence of a piston plasma over the same time intervals as in Fig. 2. The measurements yielded a time-averaged mean electron density $n_{e0} = 0.9 \pm 0.2 \times 10^{18}$ cm^{-3} and temperature $T_{e0} = 40 \pm 10$ eV [35].

The spectra show qualitative signatures of a magnetized collisionless shock precursor, and can be divided into four distinct regions in the IAW spectra, labeled I–IV in Fig. 2(a). Region I consists of piston ions that are streaming through the ambient plasma (region II) but largely

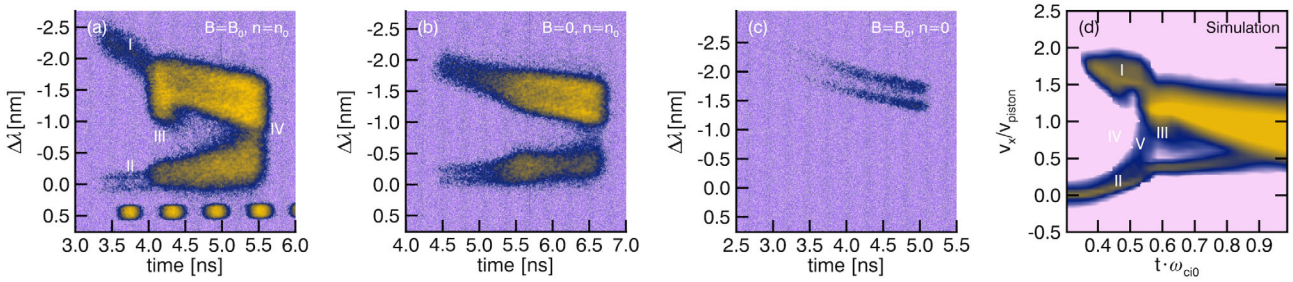

F2:1 FIG. 2. IAW spectra of piston-ambient interactions under three experimental conditions: (a) magnetized ambient plasma,
F2:2 (b) unmagnetized ambient plasma, and (c) no ambient plasma. Data in (a) and (c) were taken at $x = 3$ mm (TCC), while in (b) were
F2:3 taken at $x = 4$ mm. The wavelength shift $\Delta\lambda$ is relative to the probe beam, and the marks at the bottom of (a) are timing fiducials.
F2:4 (d) Simulated ion velocity space in conditions similar to (a), with velocity relative to the piston speed and time relative to the upstream
F2:5 gyrofrequency. Regions of interest are labeled with Roman numerals and discussed in the text.

unaffected by the magnetic field. A key step in piston-driven shock formation is the sweeping up of ambient plasma [36] and the resulting compression of the magnetic field.

The increased field then causes a pileup of piston plasma and deformation of the piston flow. Both the ambient ion acceleration and piston deformation are seen in region III, which also corresponds to the peak in the EPW spectra in Fig. 3(a). Eventually, most of the ambient ions not participating in shock formation are swept up by the piston, which results in the merging of the piston and ambient plasmas in region IV. Without a background magnetic field [Fig. 2(b)], no ion pileup or flow deformation is observed, though the ambient ions are still eventually swept up. Likewise, Fig. 2(c) shows that with only a magnetized piston plasma, no shock precursor forms. These last two cases indicate that the presence of both the ambient plasma and background field is critical to shock formation. Lastly, Fig. 2(d) is the x component of the ion velocity distribution in the Thomson-scattering volume as a function of time from a 1D multispecies (CH) PSC [37,38] particle-in-cell simulation under conditions similar to Fig. 2(a). The four regions of Fig. 2(a) are clearly visible in the simulation and show that there is strong correspondence between the velocity distributions and the Thomson-scattered spectra. The simulation also shows additional features due to the H plasma (region V), but calculations indicate that the H ion acoustic waves would be heavily Landau damped relative to the C waves and so would not be observable.

Figure 3(c) shows a 14.7 MeV proton image taken at $t_0 + 3.75$ ns under the same conditions as Fig. 2(a). White, high-fluence and dark, low-fluence shells that result from the deflection of protons by the B_y magnetic field can be clearly seen, and represent large gradients in the path-integrated magnetic fields. Since there is no evidence at this late time of large-scale proton deflections due the expansion of the ambient plasma, the observed features primarily represent the 2D projection of the 3D magnetic cavity created by the expanding piston plasma. In Fig. 3(d), along a 1D profile through TCC [red box in Fig. 3(c)], we invert the proton fluence profile (red squares) [39] to reconstruct the path-integrated magnetic field $\int B_y dz$ (black line). The result indicates that magnetic flux has been swept up into a thin shell, consistent with an expanding piston. To unfold the original field, we assume a simple 3D model $B_y(x, y, z)$ for the magnetic cavity [40] and iteratively fit the model parameters to find the best match between the model-generated synthetic fluence and measured fluence.

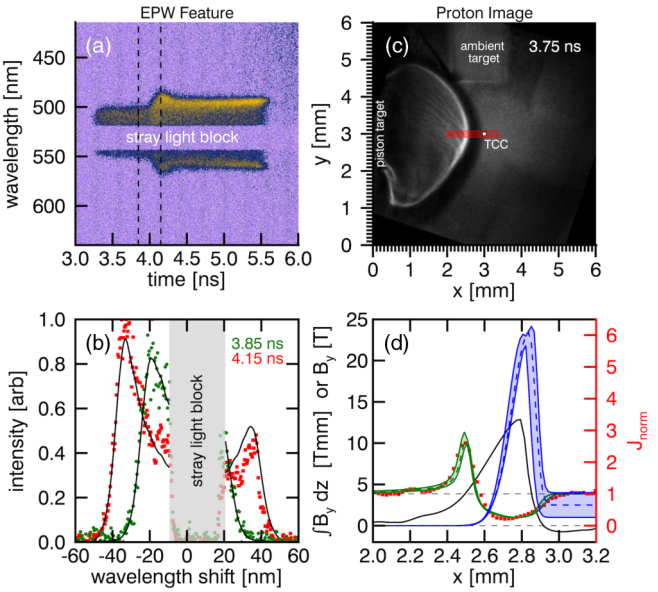

F3:1 FIG. 3. (a) Streaked Thomson-scattered spectrum of the EPW feature taken at TCC, corresponding to Fig. 2(a). (b) Two
F3:2 example profiles at time $t_0 + 3.85$ ns (green) and $t_0 + 4.15$ ns
F3:3 (red), along with best fits (black). (c) Proton radiography image
F3:4 taken at time $t_0 + 3.75$ ns using 14.7 MeV protons. (d) Proton
F3:5 intensity (red squares) taken from the red region in (c), normal-
F3:6 ized to the mean intensity, and the associated reconstructed
F3:7 path-integrated magnetic field $\int B_y dz$ (black). Also shown is the
F3:8 normalized proton intensity (green dashed) forwarded-modeled
F3:9 from a 2D synthetic magnetic field $B_y(x, z)$, which has the dashed
F3:10 blue profile at $z = 0$. The model uncertainties are shown as
F3:11 shaded regions.
F3:12

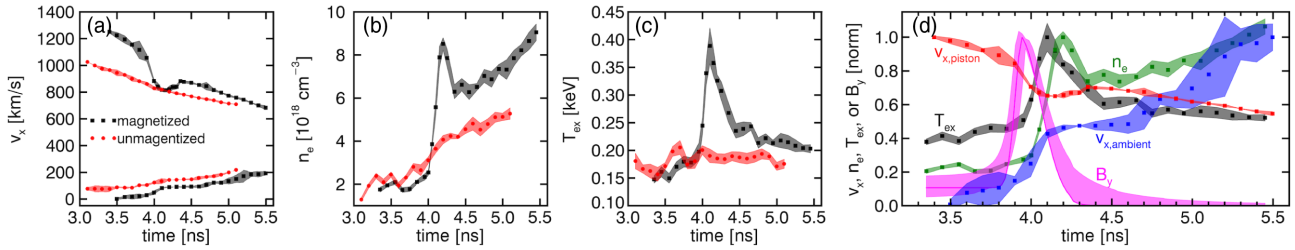

F4:1 FIG. 4. Thomson scattering results. Measured (a) piston and ambient ion flow speed v_x, (b) electron density n_e, and (c) electron
F4:2 temperature T_{ex} for a piston plasma expanding through a magnetized (black squares) and unmagnetized (red circles) ambient plasma.
F4:3 (d) Electron temperature (black), density (green), magnetic field (magenta), and piston (red) and ambient (blue) ion flow speed for the
F4:4 magnetized case. The magnetic field profile was constructed from the model in Fig. 3(d). Error bars are shown as shaded regions. The
F4:5 magnetized plasma were probed at $x = 3$ mm (TCC), while the unmagnetized plasma was probed at $x = 4$ mm. The unmagnetized data
F4:6 have been shifted forward in time by 1.5 ns for ease of comparison.

The best fit synthetic fluence (green line) is shown in Fig. 3(d), along with the corresponding model field $B_y(x)$ (blue line) that passes through the location of the Thomson scattering measurements. Here, the model field has a peak value $B_{y,\mathrm{peak}} = 23 \pm 2$ T at $x_{\mathrm{peak}} = 2.85 \pm 0.05$ mm, though the local upstream value $B_{y0} = 3 \pm 2$ T is not well constrained. Comparison of the 3 and 14.7 MeV protons images also indicates that the protons are not significantly deflected by electric fields [40].

We can further quantify the Thomson-scattered spectra in Figs. 2 and 3 by iteratively fitting the data with a spectral model of the scattered power [33] to extract the time-resolved electron density n_e and x component of the electron temperature T_{ex} and ion flow speed v_x. An example EPW spectrum and fit is shown in Fig. 3(b). To perform error analysis, we employ a Monte Carlo approach in which the extracted plasma parameters represent the mean value over 50 fits, with error bars corresponding to the standard deviation. In all cases, the EPW spectral fits assumed Maxwellian velocity distributions. In contrast, the IAW spectra involve multiple ion species (C and H) and multiple flows from potentially non-Maxwellian ion distributions. Extracting parameters from these spectra is beyond the scope of this Letter and will be reported separately. Instead, we only determine the ion flow speed from the Doppler shifts of the spectra, which can be accurately resolved without knowing the exact form of the scattered power [18]. Based on the results of these fits (see Fig. 4), we can justify the use of Maxwellian distributions by estimating the electron τ_{ee} and electron-ion τ_{ei} collision times relative to the fastest gradient timescales $\tau_s \sim 200$ ps and the electron plasma frequency ω_{pe}. We find for the electrons that $\tau_{ee} < \tau_s$, indicating that the electrons are well thermalized, and that $\tau_{pe} \ll \tau_{ei} < \tau_{ee}$, so that collisions do not significantly affect the EPW spectra. Furthermore, the spatial scales are dominantly determined by the piston-ambient ion (and eventually ambient-ambient ion) interaction, which is highly collisionless ($\tau_{pa}/\tau_s \ggg 1$) due the large flow velocities in these experiments.

A summary of the Thomson scattering results is shown in Fig. 4 for magnetized (black) and unmagnetized (red) piston-ambient interactions. Figure 4(a) shows two sets of flow speeds v_x extracted from the IAW spectra that correspond to the faster (piston) and slower (ambient) moving populations. For the magnetized case, the piston ions exhibit a rapid deceleration around $t_0 + 4.0$ ns, coincident with the onset of the region of ion pileup in Fig. 2(a). Over the same time the ambient ions are accelerated, and then plateau for several hundred ps before being accelerated again as they begin to merge with the piston plasma. In the unmagnetized case, the piston ions show no deceleration and are consistent with a free-streaming expansion ($v \propto 1/t$). Figures 4(b) and 4(c) show electron density and temperature extracted from the EPW spectra. In the region of ion pileup, the magnetized case exhibits a strong density compression $n_e/n_{e0} \approx 10$, steep density ramp $\tau_n \sim 200$ ps, and electron heating $T_{ex}/T_{e0} \approx 10$, where n_{e0} and T_{e0} are the density and temperature in the stand-alone ambient plasma. The shock precursor has a time-of-flight speed of $v_{sh} \approx 750$ km/s, corresponding to an acoustic Mach number $M_s = v_{sh}/C_{s,C} \approx 15$, where $C_{s,C}$ is the upstream C ion sound speed evaluated at T_{e0}. No density compression or electron heating is observed in the unmagnetized case.

Figure 4(d) combines temperature (black), density (green), magnetic field (purple), and piston (red) and ambient (blue) ion flow results for the magnetized case. The field is plotted assuming that it is slowly changing on the timescales of interest, so that the spatial profile can be converted to a temporal profile using the time-of-flight speed $v_{\mathrm{field}} = 760 \pm 20$ km/s. The combined profiles directly demonstrate the piston-ambient ion coupling that is critical to shock formation. First, the magnetic field acts as an interface between the highly magnetized ambient and piston electrons: swept-over ambient electrons compress the field at the leading edge while piston electrons expel the field [41]. Consequently, the piston electrons (and ions) will necessarily pile up behind the magnetic compression, as observed. This results in a localized electron density peak that then transitions into the smooth ablation profile of

the piston plume. The temperature in turn rises adiabatically ($T_e \propto n_e^{2/3}$) with the density, consistent with collisional electrons.

While at this stage in formation the density profile primarily reflects piston dynamics, it also crucially leads to the sweeping up of ambient ions through the pressure gradient electric field $E_P = -\nabla P_e/en_e$, where $P_e = n_e T_e$, and the magnetic gradient field $E_B = -\nabla B^2/2\mu_0 en_e$. As seen in Fig. 4(d), the change in ambient ion speed between 3.75 and 4.15 ns is $\Delta v \sim 66$ km/s. Assuming that gradients of the temporally or spatially varying functions f can be related through $df/dx \approx (1/v_{\text{field}})df/dt$, we can estimate the effect of these fields on the ambient ions from our measured data. Over the same time range, the pressure gradient field accelerates the ions by $\Delta v_{EP} = \int (Z_C e/m_C) E_P dt \approx 38$ km/s, while the magnetic gradient field accelerates the ions by $\Delta v_{EB} \approx 19$ km/s, giving a combined change $\Delta v_E \approx 57$ km/s that agrees well with the measurements. The relative contributions are also consistent with the $\beta_e = 2\mu_0 P_e/B^2 > 1$ conditions in these experiments, since $E_P/E_B \propto \beta_e$. While the magnitude of these electric fields has been measured [42] or inferred from simulations [36] in previous $\beta_e < 1$ piston-ambient coupling experiments, this is the first time that they have been estimated directly from localized measurements when $\beta_e > 1$. The piston ion flow is correspondingly affected by the electric fields, decelerating slightly behind the density compression, and then strongly accelerating at the leading edge. The deformation of the ion flows is therefore a key signature of the onset of piston-driven shock formation.

In summary, we have measured for the first time through Thomson scattering the evolution of electron and ion velocity distributions in magnetized collisionless shock precursors. We have extracted time-resolved profiles of electron temperature, density, and ion flow speed, which indicate the development of strong density compressions and electron heating associated with the pileup of piston ions and acceleration of ambient ions by magnetic and pressure gradient electric fields. Proton radiography images confirm that there is an associated strong magnetic compression in the same region. This acceleration of ambient ions and subsequent deformation of the piston ion flow is a key component of magnetized shock formation, and is not observed without both a background magnetic field and ambient plasma. Since the distributions can in principle be probed along any direction, these results will enable future experiments to study multidimensional distribution functions in a manner analogous to spacecraft, allowing direct comparisons between studies of space and laboratory collisionless shocks.

We thank the staff of the Omega facility for their help in executing these experiments. Time at the Omega facility was funded by the Department of Energy (DOE) through Grant No. DE-NA0003613. Processing of the proton images was funded by the DOE under Grant No. DE-FG03-09NA29553. Simulations were conducted on the Titan supercomputer at the Oak Ridge Leadership Computing Facility at the Oak Ridge National Laboratory through the Innovative and Novel Computational Impact on Theory and Experiment (INCITE) program, which is supported by the Office of Science of the DOE under Contract No. DE-AC05-00OR22725. This research was also supported by the DOE under Grants No. DE-SC0008655 and No. DE-SC0016249.

*dereks@princeton.edu

[1] E. J. Smith, L. Davis, D. E. Jones, P. J. Coleman, D. S. Colburn, P. Dyal, and C. P. Sonett, Science **188**, 451 (1975).
[2] E. J. Smith, L. Davis, D. E. Jones, P. J. Coleman, D. S. Colburn, P. Dyal, and C. P. Sonett, Science **207**, 407 (1980).
[3] A. H. Sulaiman, A. Masters, M. K. Dougherty, D. Burgess, M. Fujimoto, and G. B. Hospodarsky, Phys. Rev. Lett. **115**, 125001 (2015).
[4] P. J. Cargill and K. Papadopoulos, Astrophys. J. Lett. **329**, L29 (1988).
[5] D. S. Spicer, S. P. Maran, and R. W. Clark, Astrophys. J. **356**, 549 (1990).
[6] A. Bamba, R. Yamazaki, M. Ueno, and K. Koyama, Astrophys. J. **589**, 827 (2003).
[7] M. Balikhin, M. Gedalin, and A. Petrukovich, Phys. Rev. Lett. **70**, 1259 (1993).
[8] B. Lembège, P. Savoini, M. Balikhin, S. Walker, and V. Krasnoselskikh, J. Geophys. Res. **108**, 1256 (2003).
[9] S. J. Schwartz, E. Henley, J. Mitchell, and V. Krasnoselskikh, Phys. Rev. Lett. **107**, 215002 (2011).
[10] D. Burgess and M. Scholer, *Collisionless Shocks in Space Plasmas: Structure and Accelerated Particles*, Cambridge Atmospheric and Space Science Series (Cambridge University Press, Cambridge, England, 2015).
[11] L.-J. Chen *et al.*, Phys. Rev. Lett. **120**, 225101 (2018).
[12] V. V. Lobzin, V. V. Krasnoselskikh, J.-M. Bosqued, J.-L. Pinçon, S. J. Schwartz, and M. Dunlop, Geophys. Res. Lett. **34**, L05107 (2007).
[13] A. Johlander *et al.*, Phys. Rev. Lett. **117**, 165101 (2016).
[14] G. G. Howes, Phys. Plasmas **25**, 055501 (2018).
[15] C. Niemann, W. Gekelman, C. G. Constantin, E. T. Everson, D. B. Schaeffer, A. S. Bondarenko, S. E. Clark, D. Winske, S. Vincena, B. Van?Compernolle, and P. Pribyl, Geophys. Res. Lett. **41**, 7413 (2014).
[16] D. B. Schaeffer, W. Fox, D. Haberberger, G. Fiksel, A. Bhattacharjee, D. H. Barnak, S. X. Hu, and K. Germaschewski, Phys. Rev. Lett. **119**, 025001 (2017).
[17] D. H. Froula, J. S. Ross, L. Divol, and S. H. Glenzer, Rev. Sci. Instrum. **77**, 10E522 (2006).
[18] J. Sheffield, D. H. Froula, S. H. Glenzer, and N. Luhmann, *Plasma Scattering of Electromagnetic Radiaiton*, 2nd ed. (Academic Press, New York, 2011).
[19] J. W. M. Paul, G. C. Goldenbaum, A. Iiyoshi, L. S. Holmes, and R. A. Hardcastle, Nature (London) **216**, 363 (1967).
[20] A. W. DeSilva and J. A. Stamper, Phys. Rev. Lett. **19**, 1027 (1967).

[21] L. G. Suttle, J. D. Hare, S. V. Lebedev, G. F. Swadling, G. C. Burdiak, A. Ciardi, J. P. Chittenden, N. F. Loureiro, N. Niasse, F. Suzuki-Vidal, J. Wu, Q. Yang, T. Clayson, A. Frank, T. S. Robinson, R. A. Smith, and N. Stuart, Phys. Rev. Lett. **116**, 225001 (2016).

[22] H. G. Rinderknecht, H.-S. Park, J. S. Ross, P. A. Amendt, D. P. Higginson, S. C. Wilks, D. Haberberger, J. Katz, D. H. Froula, N. M. Hoffman, G. Kagan, B. D. Keenan, and E. L. Vold, Phys. Rev. Lett. **120**, 095001 (2018).

[23] J. S. Ross, H.-S. Park, R. Berger, L. Divol, N. L. Kugland, W. Rozmus, D. Ryutov, and S. H. Glenzer, Phys. Rev. Lett. **110**, 145005 (2013).

[24] T. Morita, Y. Sakawa, K. Tomita, T. Ide, Y. Kuramitsu, K. Nishio, K. Nakayama, K. Inoue, T. Moritaka, H. Ide, M. Kuwada, K. Tsubouchi, K. Uchino, and H. Takabe, Phys. Plasmas **20**, 092115 (2013).

[25] D. B. Schaeffer, E. T. Everson, D. Winske, C. G. Constantin, A. S. Bondarenko, L. A. Morton, K. A. Flippo, D. S. Montgomery, S. A. Gaillard, and C. Niemann, Phys. Plasmas **19**, 070702 (2012).

[26] D. B. Schaeffer, W. Fox, D. Haberberger, G. Fiksel, A. Bhattacharjee, D. H. Barnak, S. X. Hu, K. Germaschewski, and R. K. Follett, Phys. Plasmas **24**, 122702 (2017).

[27] G. Fiksel, W. Fox, A. Bhattacharjee, D. H. Barnak, P.-Y. Chang, K. Germaschewski, S. X. Hu, and P. M. Nilson, Phys. Rev. Lett. **113**, 105003 (2014).

[28] W. Fox, G. Fiksel, A. Bhattacharjee, P.-Y. Chang, K. Germaschewski, S. X. Hu, and P. M. Nilson, Phys. Rev. Lett. **111**, 225002 (2013).

[29] T. R. Boehly, R. S. Craxton, T. H. Hinterman, J. H. Kelly, T. J. Kessler, S. A. Kumpan, S. A. Letzring, R. L. McCrory, S. F. B. Morse, W. Seka, S. Skupsky, J. M. Soures, and C. P. Verdon, Rev. Sci. Instrum. **66**, 508 (1995).

[30] G. Fiksel, A. Agliata, D. Barnak, G. Brent, P.-Y. Chang, L. Folnsbee, G. Gates, D. Hasset, D. Lonobile, J. Magoon, D. Mastrosimone, M. J. Shoup, and R. Betti, Rev. Sci. Instrum. **86**, 016105 (2015).

[31] C. Niemann, W. Gekelman, C. G. Constantin, E. T. Everson, D. B. Schaeffer, S. E. Clark, D. Winske, A. B. Zylstra, P. Pribyl, S. K. P. Tripathi, D. Larson, S. H. Glenzer, and A. S. Bondarenko, Phys. Plasmas **20**, 012108 (2013).

[32] D. B. Schaeffer, L. R. Hofer, E. N. Knall, P. V. Heuer, C. G. Constantin, and C. Niemann, High Power Laser Sci. Eng. **6**, e17 (2018).

[33] R. K. Follett, J. A. Delettrez, D. H. Edgell, R. J. Henchen, J. Katz, J. F. Myatt, and D. H. Froula, Rev. Sci. Instrum. **87**, 11E401 (2016).

[34] R. D. Petrasso, C. K. Li, F. H. Seguin, J. R. Rygg, J. A. Frenje, R. Betti, J. P. Knauer, D. D. Meyerhofer, P. A. Amendt, D. H. Froula, O. L. Landen, P. K. Patel, J. S. Ross, and R. P. J. Town, Phys. Rev. Lett. **103**, 085001 (2009).

[35] Because of heating of the electrons by the probe beam for temperatures less than 100 eV (see for example Ref. [18]), these measurements are most likely an overestimate of the true electron temperature.

[36] A. S. Bondarenko, D. B. Schaeffer, E. T. Everson, S. E. Clark, B. R. Lee, C. G. Constantin, S. Vincena, B. Van Compernolle, S. K. P. Tripathi, D. Winske, and C. Niemann, Nat. Phys. **13**, 573 (2017).

[37] K. Germaschewski, W. Fox, S. Abbott, N. Ahmadi, K. Maynard, L. Wang, H. Ruhl, and A. Bhattacharjee, J. Comput. Phys. **318**, 305 (2016).

[38] W. Fox, J. Matteucci, C. Moissard, D. B. Schaeffer, A. Bhattacharjee, K. Germaschewski, and S. X. Hu, Phys. Plasmas **25**, 102106 (2018).

[39] A. F. A. Bott, C. Graziani, P. Tzeferacos, T. G. White, D. Q. Lamb, G. Gregori, and A. A. Schekochihin, J. Plasma Phys. **83**, 905830614 (2017).

[40] See Supplemental Material at http://link.aps.org/supplemental/10.1103/PhysRevLett.000.000000 for more information on the analysis of the proton radiography images.

[41] T. P. Wright, Phys. Fluids **14**, 1905 (1971).

[42] J. Bonde, S. Vincena, and W. Gekelman, Phys. Plasmas **25**, 042110 (2018).